

1 **Testing ground based observations of wave activity in the (lower and upper) atmosphere**
2 **as possible (complementary) indicators of streamer events**

3 **Michal Kozubek¹, Lisa Kuchelbacher², Jaroslav Chum¹, Tereza Sindelarova¹, Franziska**
4 **Trinkl^{2, a}, Katerina Podolska¹**

5 ¹Institute of Atmospheric Physics CAS, Bocni II 1401, Prague, 14100, Czech Republic

6 ² Earth Observation Center, Deutsches Zentrum für Luft- und Raumfahrt, 82234 Weßling,
7 Germany

8 ^a now at Karlsruhe Institute of Technology (KIT), Institute of Meteorology and Climate
9 Research, Karlsruhe, Germany

10 **Correspondence: Michal Kozubek, kom@ufa.cas.cz**

11 **Keywords:** gravity waves, streamer events, infrasound, Doppler measurements

12

13 **Abstract:** For a better understanding of atmospheric dynamics, it is very important to know
14 the general condition (dynamics and chemistry) of the atmosphere. Planetary waves (PWs) are
15 global scale waves, which are well-known as main drivers of the large-scale weather patterns
16 in mid-latitudes on time scales from several days up to weeks in the troposphere. When PWs
17 break, they often cut pressure cells off the jet stream. A specific example are so-called
18 streamer events, which occur predominantly in the lower stratosphere at mid- and high-
19 latitudes. For streamer events we check, whether there are any changes of gravity wave (GW)
20 or infrasound characteristics related to these events in ionospheric and surface measurements
21 (continuous Doppler soundings, two arrays of microbarometers) in the Czech Republic.
22 Different phenomena were identified in infrasound arrival parameters at the respective surface
23 infrasound stations and also during the respective analysed streamer events. The streamers
24 signatures in infrasound observations are variable, because the location of the events and their
25 impact on the tropopause – lower stratosphere region differs from event to event.
26 Supplementary ground-based measurements of GW using the WBCI array in the troposphere
27 showed that GW propagation azimuths were more random during streamer and streamer-like
28 events compared to those observed during calm conditions. GW propagation characteristics
29 observed in the ionosphere by continuous Doppler soundings during streamer events did not
30 differ from those expected for the given time period.

31

32 1) Introduction

33 For a better comprehension of climate change it is fundamentally important, how well we
34 understand the climate system in general, and the dynamics of the atmosphere in particular.
35 The dynamical processes relevant in this context in the atmosphere take place over a
36 comparatively wide range of scales in space and time. They include in particular both,
37 planetary and gravity waves. Planetary waves are the main drivers of the extratropical
38 circulation. When they break, they lead to an irreversible exchange of air masses between the
39 equatorial and polar region due to an amplification of their amplitudes (e.g. McIntyre &
40 Palmer, 1983; Polvani & Plumb, 1992). In the lower stratosphere ozone can be used as a tracer
41 for these large-scale motions, as it has a comparatively long life-time. When planetary waves
42 break tropical air masses of low ozone concentration are mixed poleward into the
43 surrounding atmosphere of the mid and higher latitudes (e.g. Leovy et al., 1985).

44 The term "streamer" lacks a precise definition, as noted by Krüger et al. (2005). They
45 discuss various aspects of streamers, including their impact on mixing and the divergent
46 definitions associated with them. Offermann et al. (1999) describe streamers as large-scale
47 tongue-like structures formed by the meridional deflection of air masses. Streamers are
48 characterized by irreversible mixing of air masses between equatorial and polar regions which
49 is why they might be linked to planetary wave breaking (Vaugh, 1993). Eyring et al. (2003)
50 give a climatology of the seasonal and geographical distribution of streamer events. They
51 show, that streamers often occur over the Northern Atlantic and can be identified by either
52 high NO₂ or low ozone concentration, which is why we select streamers by total ozone
53 column measurements. They show that streamer events occur most often during winter and
54 least during July and August in the Northern Hemisphere. During a streamer event the wind
55 field changes rather strong over a comparatively small distance. Since a streamer event shows
56 a strong wind shear at its flanks, it is expected that it excites GW (e.g. Kramer et al., 2015 and
57 2016 or Peters et al., 2003).

58 It is well-known that enhanced wind gradients or anticyclones can lead to the
59 excitation of gravity waves (GW) in the atmosphere (e.g. Pramitha et al., 2015; Kai et al.,
60 2010; Kramer et al., 2015, 2016 and Gerlach et al., 2003). GW have typical vertical
61 wavelengths from a few 100 m to several kilometres (Wüst & Bittner, 2006), and horizontal
62 wavelengths over tens of km (Wüst et al., 2018), and longer (Rauthe et al., 2006); their
63 fluctuations in the upper troposphere / lower stratosphere typically show amplitudes of 5–10

64 m/s at maximum (e.g., Kramer et al., 2015). Those waves transport energy and momentum
65 horizontally and vertically through the atmosphere and deposit them especially in the
66 stratosphere and mesosphere but also above and below this height region. The propagation of
67 GWs is strongly dependent on the wind conditions in the stratosphere since the wind speed of
68 the middle atmosphere (10–100 km) reaches its maximum there. That is why monitoring
69 waves in upper parts of the atmosphere, e.g. based on Doppler observations in the ionosphere,
70 can provide additional information about stratospheric conditions (for details see Fritts and
71 Alexander, 2003).

72 Using pressure recordings at a microbarograph array, GWs and infrasound at the ground can
73 be observed. Ground based observations of GWs at a large aperture microbarograph array are
74 utilized in the present study as an independent data source for the analysis of GW activity
75 during streamer events. Infrasound propagation is influenced by wind and temperature fields
76 in the atmosphere. Three regions play an important role in long-distance infrasound
77 propagation: (1) the lower thermosphere; (2) the stratosphere; (3) the jet stream near the
78 tropopause and inversion layers in the troposphere (Evers and Haak, 2010). Infrasound
79 observed at the ground and emitted by distant sources mostly propagates in the stratospheric
80 waveguide (Ceranna et al., 2019). The thermospheric waveguide is not as efficient as the
81 stratospheric waveguide in the long-range infrasound propagation. Besides signal loss due to
82 geometrical spreading, infrasound absorption is important in the upper atmosphere (Bittner et
83 al., 2010). Infrasound absorption is proportional to the frequency; higher frequencies,
84 particularly those above 1 Hz undergo stronger absorption in the thermosphere (Sutherland
85 and Bass, 2004). Signal attenuation is low at frequencies of the order of $10^{-3} - 10^{-2}$ Hz (Blanc,
86 1985; Georges, 1968).

87 A number of case studies have proved that stratospheric dynamics can be deduced from
88 microbarograph measurements at the ground (Assink et al., 2014; Blixt et al., 2019; Evers and
89 Siegmund, 2009; Evers et al., 2012; Garcès et al., 2004; Le Pichon and Blanc, 2005; Le
90 Pichon et al., 2006 and 2009; Smets and Evers, 2014). Streamer events are significant
91 transient disturbances to circulation patterns in the tropopause/lower stratosphere region;
92 modifications of the stratospheric waveguide can therefore be expected. A feasibility study on
93 utilisation of ground infrasound measurements in research of streamer events is performed. Its
94 aim is to identify phenomena in infrasound detections related to the streamers; we focus on
95 deviations of the azimuth of signal arrivals, trace velocity, signal amplitude, and frequency.
96 The dedicated studies demonstrated that from the observed signal trace velocity, information

97 about the signal refraction height can be derived (Lonzaga, 2015). If the source of received
98 signals is well defined in time and space, mean atmospheric cross-winds along the signal
99 propagation path can be estimated from back-azimuth deviations and time of signal
100 propagation (Blixt et al., 2019). Fluctuations of signal frequency and amplitude are, besides
101 variability of the signal source influenced by atmospheric filtering (Sutherland and Bass,
102 2004).

103 Our study will focus on possible utilization Doppler sounding and microbarographs for
104 description and analysis of GW behaviour and propagation in the stratosphere.

105 The structure of the paper is as follows: After introduction the description of the used dataset
106 and method can be found in the second section. Then we describe our results and in the last
107 section we discuss the possible connection to previous studies.

108

109 **2) Data and methods**

110 The selection of streamer events is based on the visual inspection of global maps of total
111 ozone column (TO3), accessible through a service provided by DLR
112 (<https://atmos.eoc.dlr.de/>) measured by the Tropospheric Monitoring Instrument (TROPOMI)
113 aboard the Sentinel 5 Precursor (S5P) mission. See Veefkind et al., 2012 for details about
114 TROPOMI/S5P. In cases where TROPOMI/S5P data is unavailable, measurements from the
115 Global Ozone Monitoring Experiment-2 (GOME-2) on the Metop series of satellites are
116 utilized. Both instruments operate in a nadir-viewing configuration on near-polar sun-
117 synchronous orbits. Further specifics regarding TO3 measurements by TROPOMI/S5P are
118 elaborated by Spurr et al. (2022). The TO3 retrieval process is built upon the predecessor
119 instrument's processor, with GOME-2 on Metop-AB, see Munro et al. (2006) and Munro et al.
120 (2016). For detailed information on the GOME-2 retrieval algorithm, refer to Loyola et al.
121 (2011).

122 We define a streamer as such when the ozone column concentration of the finger-like
123 structure above the Northern Atlantic/Western Europe is lower than 300 DU and persists for
124 at least 3 days. The longitudinal extension is of approx. 15 to 30 degrees in the mid-latitudes
125 (between 30 to 70°N). The northernmost point of a streamer exceeds 50°N. Fig. 1 shows a
126 streamer event above the Northern Atlantic, indicated by the blue color which represent the

127 low ozone concentrations. The streamer shown in Fig. 1 reaches latitudes beyond 70°N,
128 which indicates a large example. At the western and eastern flanks of the streamer, the ozone
129 concentration exceeds 350 DU, defining distinct boundaries. This is also visible in Fig. 1
130 represented by the green colors at the eastern coast of Northern America and western Europe.
131 So, there is a gradient of the ozone concentration of about 50 DU / 5°. Furthermore, the
132 streamer exhibits a discernible pattern of circulation, with air masses being meridionally
133 deflected, contributing to its formation and maintenance. These air masses, characterized by
134 their movement from south to north at the eastern flank and from north to south at the western
135 flank, play a significant role in the streamer's dynamics. This is the reason why equatorial low
136 ozone concentration is transported northward. In contrast, the calm periods, representing the
137 opposite dynamic situation to the streamer events, are characterized by only very few
138 meridionally deflected air masses. During these periods, the ozone concentration in the mid-
139 latitudes above the Northern Atlantic is consistently higher than 350 DU, indicating stable
140 atmospheric conditions and minimal perturbations in the ozone distribution. An example for a
141 calm period is shown in Fig. 2.

142 The streamer events are selected by eye for this study (results see [Error! Reference source](#)
143 [not found, Table 4](#)) considering the TO3 global maps from January 2020 and March 2021. As
144 planetary waves are permanently disturbing the atmospheric dynamic of the higher
145 troposphere / lower stratosphere, especially smaller scale streamers can be observed almost
146 every day and the identification of streamer events becomes subjective. We therefore focus on
147 few events which are comparatively strong in their evolution from our perspective. Moreover,
148 we focus on streamer events above the Northern Atlantic. Whenever another streamer event
149 occurs somewhere other than over the Northern Atlantic region with comparable
150 spatiotemporal extent, we do not consider this date as a streamer event. We assume that the
151 effects of the streamer superimpose and a distinct backtrack to the streamer over the Northern
152 Atlantic will not be possible. This means, that the analysis of the streamer events can be
153 blurred to some extent.

154 We consider dates from January 2020 to April 2021. In general, planetary waves drive the
155 Brewer Dobson Circulation in the stratosphere during winter and ozone-poor airmasses are
156 transported northward. Streamer events are therefore detected between September and March.
157 The streamer events are distinguished if they have a large spatial size, high intensity (low
158 TO3 concentration) and if air masses are irreversibly mixed into the surrounding atmosphere.
159 All the selected events persist for several days, but no longer than 10 days.

160 To evaluate whether streamer events effect the smaller-scale atmospheric dynamics, calm
 161 events are identified as well by subjective criteria. These events serve as a reference to
 162 streamer events, as large-scale spatial structures are hardly visible in the TO3. The events are
 163 selected when the ozone concentration shows a meridional gradient from the equator to polar
 164 region on the Northern Hemisphere with almost no longitudinal variation. The examples of
 165 calm atmospheric dynamics are listed in Table 1 (right).

166

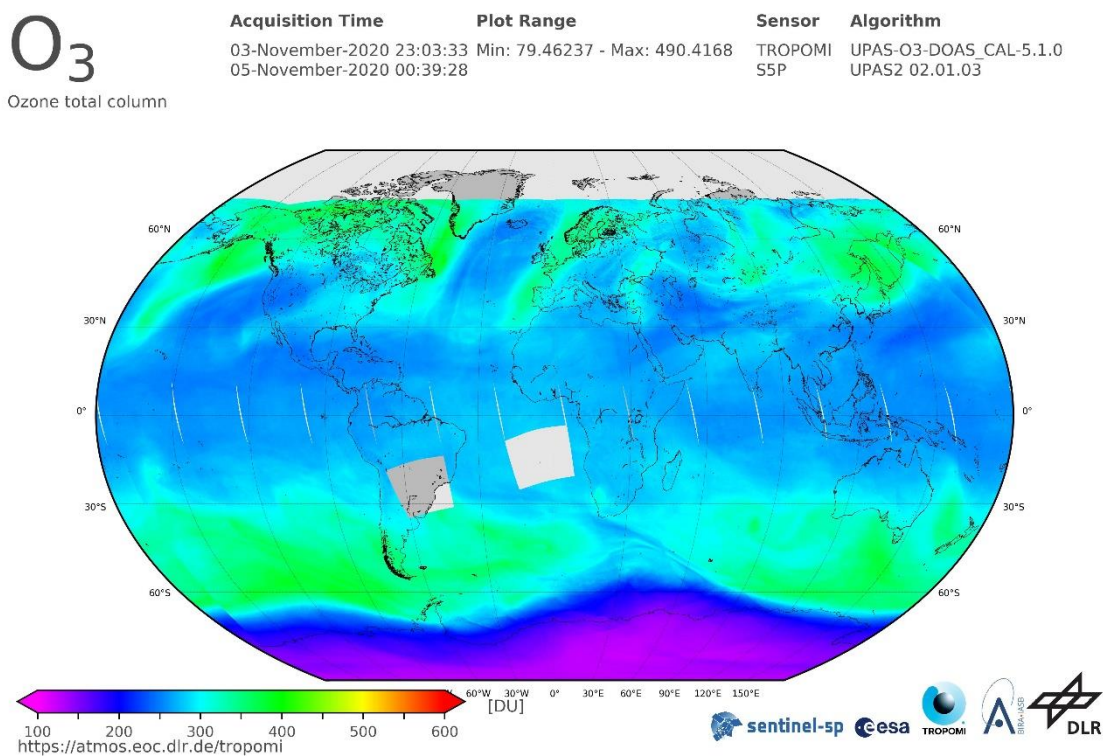
Streamer events		Calm periods	
From	To	From	To
06.02.2020	10.02.2020	02.03.2020	08.03.2020
11.2.2020	13.2.2020	09.03.2020	14.03.2020
31.08.2020	03.09.2020	28.03.2020	10.04.2020
05.09.2020	11.09.2020	19.04.2020	27.05.2020
03.11.2020	07.11.2020	9.11.2020	15.11.2020
21.11.2020	25.11.2020	12.12.2020	22.12.2020
23.02.2021	27.02.2021	30.12.2020	06.01.2021
09.03.2021	12.03.2021	21.01.2021	20.02.2021
		28.02.2021	07.03.2021
		13.03.2021	24.03.2021
		29.03.2021	07.04.2021

167 **Table 1** Streamer events above Northern Atlantic from January 2020 until March 2021 and
 168 related start and end dates. The right part shows calm periods.

169

170 Figure 1 shows the TO3 by TOPOMI/S5P integrated from November 3rd to November 5th
 171 2020. Ozone-poor airmasses (blue) are located above the Northern Atlantic from 30°N to
 172 70°N next to smaller scale ozone-poor airmasses above western North America and Central

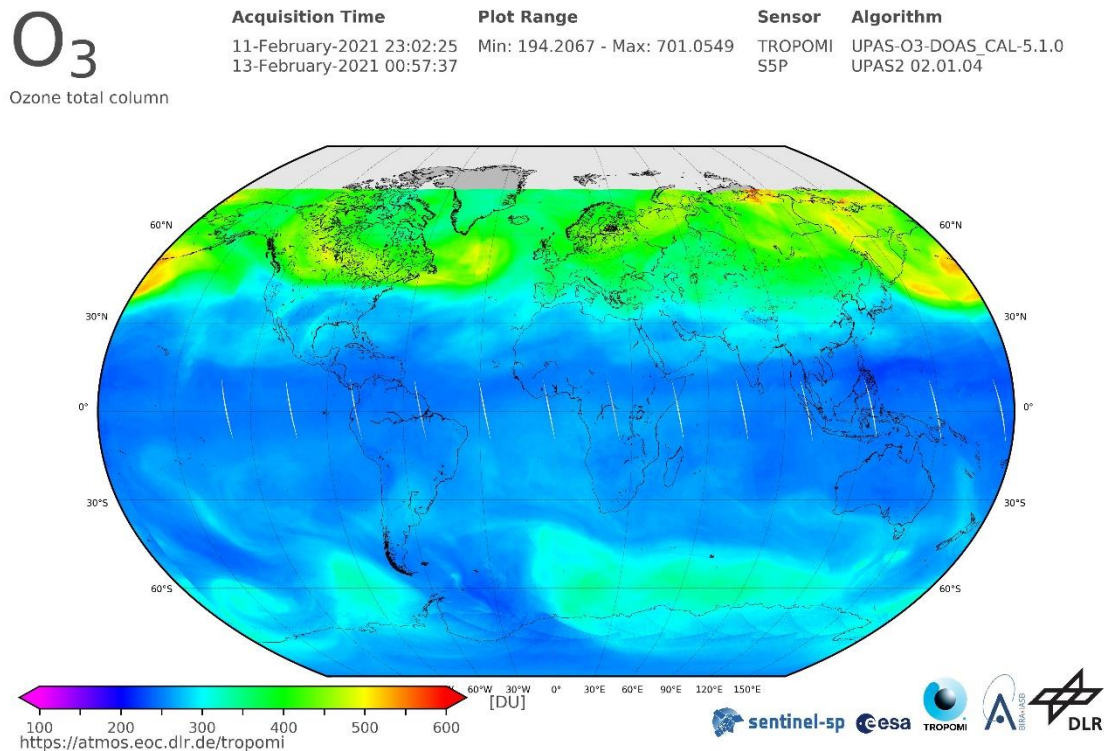
173 Asia. The TO3 concentration is disturbed by planetary waves along the latitudes, which lead
 174 to wave structures visible especially at the transition of blue to green colors. A large streamer
 175 event of ozone-poor airmasses is detected over the Northern Atlantic. A small streamer can be
 176 detected over western North America. There are also ozone-poor air masses above eastern
 177 Europe. The temporal evolution shows, that the ozone-poor air masses above eastern Europe
 178 are due to a decaying streamer which evolved several days earlier. As planetary waves are
 179 more or less permanently disturbing the atmospheric dynamics, especially smaller scale
 180 streamers can be detected almost every day. In this example, the streamer event above the
 181 Northern Atlantic is largest. Therefore, we consider this event for the further analysis.



183 Fig. 1. TO3 by TROPOMI/S5P from November 3rd to November 5th 2020 shows ozone poor
 184 airmasses above the Northern Atlantic as an example of a streamer event for the further
 185 analysis. Colors (from violet to red) indicate the total ozone column concentrations (from low
 186 to high) in Dobson Units. Source: DLR, CC-BY 3.0

187

188 Figure 2 shows the TO3 by TOPOMI/S5P from February 11th to February 13th 2020. The
 189 event is characterized by a strong meridional gradient from the equatorial to polar region on
 190 the Northern Hemisphere with almost no longitudinal variation. Therefore, we consider this
 191 event for the further analysis.



193

194 Fig. 2. TO3 by TROPOMI/S5P from February 11th to February 13th 2020 as an example of
 195 calm atmospheric dynamics. A clear meridional gradient of ozone can be observed on the
 196 Northern Hemisphere without large-scale wave structures. Colors (from violet to red) indicate
 197 the total ozone column concentrations (from low to high) in Dobson Units. Source: DLR, CC-
 198 BY 3.0

199 Two stations of the Czech microbarograph network (Bondar et al., 2022) are involved in the
 200 study – the large aperture array WBCI (50.25°N 12.44°E) and the small aperture array PPCI
 201 (50.52°N 14.57°E). To study propagation of GW and long-period infrasound (from acoustic
 202 cut-off up to about 2.5 s) pressure recordings at WBCI are utilized. Four sensors of the WBCI
 203 array are arranged in a tetragon. The inter-element distances of 4 – 10 km define an optimum
 204 performance of the array in the infrasound frequency range from the acoustic cut-off
 205 frequency of 0.0033 to 0.0068 Hz (Garcès, 2013). The WBCI array with its large inter-
 206 element distances has a unique configuration compared to the arrays of the International
 207 Monitoring System of the Comprehensive Nuclear Test Ban Treaty Organisation intended
 208 for infrasound monitoring in the frequency band of 0.02 – 4 Hz (Marty, 2019). Each array
 209 element at WBCI is equipped with an absolute microbarometer of the type Paroscientific
 210 6000-16B-IS with parts-per-billion resolution. A GPS receiver is used for time stamping. Data
 211 are stored with a sampling rate of 50 Hz. For infrasound monitoring, WBCI data are

212 resampled at 10 Hz sampling rate. To detect and analyze GW, 1-min mean values of the
 213 absolute pressure data are used.

214 The small aperture array PPCI provides optimal precision of detections in the frequency
 215 range of 0.14 – 3.4 Hz (Garcès, 2013). Three sensors are arranged in an equilateral triangle;
 216 the array aperture is 200 m. The differential sensors of the type Infrasound Gage ISGM03
 217 manufactured by the Scientific and Technical Centre give a flat response in the frequency
 218 range of 0.02 – 4 Hz. A GPS receiver is used for time stamping. The data are stored with a
 219 sampling frequency of 25 Hz. This sampling rate is also used in regular processing of
 220 infrasound detections at PPCI.

221 Infrasound detections are processed using the Progressive Multi-Channel Correlation (PMCC)
 222 detection algorithm (Cansi, 1995; Le Pichon and Cansi, 2003). PMCC analyses pressure
 223 recordings from an infrasound array and looks for coherent signals in overlapping time
 224 windows in several frequency bands (Le Pichon and Cansi, 2003). An elementary detection
 225 with the PMCC, or the detection pixel is declared in the time-frequency window, when signal
 226 correlation and consistency criteria are met. Detection pixels are grouped into the detection
 227 families based on similar time, frequency, azimuth of signal arrival, and signal trace velocity
 228 (Brachet et al., 2010). The arrival parameters of the detected infrasound are stored in the
 229 detection bulletins. The parameters of interest for the present study include time of arrival,
 230 azimuth of arrival, trace velocity, frequency, and amplitude. The PMCC configuration is set
 231 on an individual basis and is optimized for the given array (Brachet et al., 2010; Garcès, 2013;
 232 Szuberla et al., 2004); main parameters of the PMCC settings for the arrays PPCI and WBCI
 233 are given in Table 2.

Station	PPCI	WBCI
Detection range	0.09-7 Hz	0.0033-0.4 Hz
Length of the detection window; frequency dependent	412.84-6.44 s	2555-118 s
Adjacent windows overlap	95 %	90 %
Consistency	0.1 s	3 s
Azimuth tolerance for families forming	10°	3°
Family size	10-50 pixels	15-50 pixels

Frequency range analysed in the study of streamer events	0.09-0.4 Hz	0.0033-0.4 Hz
--	-------------	---------------

234

235 **Table 2.** Main parameters of PMCC configurations for the arrays PPCI and WPCI.

236

237 Infrasound propagation is modelled with the InfraGA/GeoAc raytracing tools (Blom and
 238 Waxler, 2012; Blom, 2019). InfraGA/GeoAc provides simulations of signal propagation
 239 from a point source; propagation through the range dependent atmosphere is modelled for
 240 the present study. Atmospheric characteristics are obtained from the G2S model (Drob et al.
 241 2003). Verticals profiles of temperature, zonal and meridional winds, density and pressure
 242 are an input for the InfraGA/GeoAc. The grid of profiles covers the area from 45° to 65°N
 243 and from 30°W to 22.5°E; latitudinal step is 5° and longitudinal step is 7.5°. The location of
 244 the signal sources is estimated regarding atmospheric circulation at the tropopause and in
 245 lower stratosphere above the studied region.

246 Propagation of GW in the thermosphere/ionosphere is studied using the multi-point and multi-
 247 frequency continuous Doppler sounding system located in Czechia. Its advantage is a high
 248 time resolution (around 10 s) compared with ionospheric sounders (ionosondes) that measure
 249 the profile of electron densities in the ionosphere. **The frequency shift is due to the motion and
 250 electron density changes in the ionospheric plasma, caused for example by interaction with
 251 atmospheric waves propagating in the neutral atmosphere, with which the ionosphere (above
 252 ~ 80 km) merges. The sounding radio signal reflects at the height, where its frequency
 253 matches the so called local plasma frequency, which is determined by the local electron
 254 density. Therefore, the reflection height changes during the day and depends on the sounding
 255 frequency. Significant Doppler shifts, usable for analysis, are obtained if the signal reflects
 256 from the so called F2 layer (approximately 200 – 300 km). Several sounding frequencies are
 257 used in Czechia. The 3.59 MHz sounding was mostly effective at night, while the 4.65 MHz
 258 sounding provided good daytime data during the period analyzed.** The propagation
 259 characteristics of GWs are calculated from the time delays between signals observed at the
 260 respective sounding paths (**reflection points for each** transmitter-receiver pairs) **assuming that
 261 the reflection points are in the midpoints between each transmitter and receiver. A 60 or 90
 262 min long time interval is usually used to calculate the velocities and azimuth of the observed
 263 waves.** The methods are in detail described by Chum and Podolska (2018). The two-
 264 dimensional (2-D) version (propagation analysis in horizontal plane only) is anticipated for

265 most of the studies, since a 3-D analysis requires simultaneous observation and signal
266 correlation at different frequencies, which is often not the case, especially during solar
267 minimum. Results of statistical investigation have been recently published (Chum et al.,
268 2021). Identical methods of propagation analysis have been applied to investigate
269 propagation of GWs in the troposphere based on data from large-aperture array WBCI (here
270 the time delays are related to the locations of individual microbarometers). All analyses will
271 be done with respect to the streamer events and calm periods shown in Table 1.

272 3) Results

273 3.1 Infrasound observations at ground microbarograph arrays WBCI and PPCI in 274 November 2020 and in March 2021

275 Wave activity in the infrasound frequency range of 0.0033-0.4 Hz is investigated combining
276 observations at stations WBCI and PPCI. Infrasound detections at WBCI are processed in the
277 frequency band of 0.0033 – 0.4 Hz. The operational range of the array is extended above the
278 upper limit of the optimum array range; the degraded performance of WBCI at frequencies
279 higher than 0.0068 Hz shall be considered. The upper limit of the analysed band is
280 intentionally set to 0.4 Hz to cover microbaroms. PPCI detections are analysed in the
281 frequency range of 0.09 – 0.4 Hz. The band partly overlaps with the detection range of the
282 WBCI array and at frequencies of 0.12 – 0.35 Hz it is dominated by microbaroms (e.g.,
283 Campus and Christie, 2010). Unlike WBCI, PPCI provides an optimal performance in the
284 microbarom band.

285 Microbaroms are infrasound signals generated by a non-linear interaction of ocean waves
286 travelling in opposite directions. Microbaroms form a wide peak around 0.2 Hz in infrasound
287 spectrum; their frequency corresponds to twice the frequency of sea waves. A powerful
288 source of microbaroms is located in the North Atlantic and the signals are regularly detected
289 by European stations (Hupe et al., 2019). The detection capability of microbaroms from the
290 North Atlantic is particularly high from October to March when the source becomes stronger
291 due to stormy weather above the ocean and signal propagation to the East from the source is
292 supported by the stratospheric waveguide (Landès et al., 2012). From the global point of
293 view, microbaroms are permanently present in recordings of infrasound stations worldwide.

294 We analyse infrasound observations from 3rd to 25th November 2020 and from 28th
295 February to 25th March 2021. In these time intervals adjacent streamers and calm periods
296 occurred (Table 1). Streamers and the calm period in the November 2020 time window are

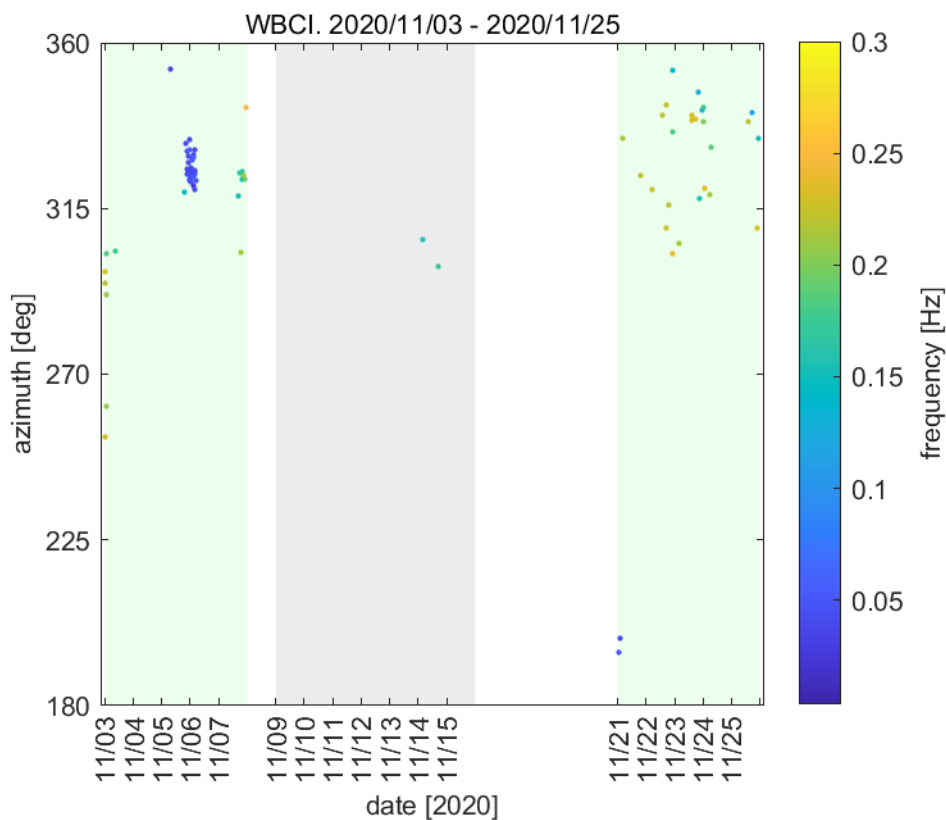
297 evaluated separately from those in the March 2021 time window to avoid seasonal
 298 influences. While a well-developed stratospheric waveguide can be expected in November,
 299 its efficiency can decrease in March due to coming seasonal reversal of stratospheric winds.
 300

301 **3.1.1 Infrasound observations from 3rd to 25th November 2020**

302 Two streamer events developed in November 2020. The first streamer occurred from 3rd
 303 to 7th November and the second one from 21st to 25th November. The streamers were
 304 separated by a calm period from 9th to 15th November.

305 WBCI provides rather sparse detections during both streamer events and only two
 306 detection families are obtained during the seven-day calm period (Figure 3). The signal
 307 frequencies near 0.2 Hz and back-azimuths of 290° – 350° indicate that the observed
 308 signals are likely microbaroms from the North Atlantic. A decrease of the signal frequency
 309 is observed during the first streamer event. On 5th – 6th November from 20 to 05 UTC, the
 310 mean frequency of the north-west arrivals drops down to 0.04 Hz. Changing signal
 311 frequencies do not occur during the second streamer from 21st to 25th November.

312



313

314 Fig. 3. Infrasound observations at WBCI on 3rd - 25th November 2020. Azimuth of signal
 315 arrivals is shown; the colorbar refers to the mean frequency of the detection family. One circle

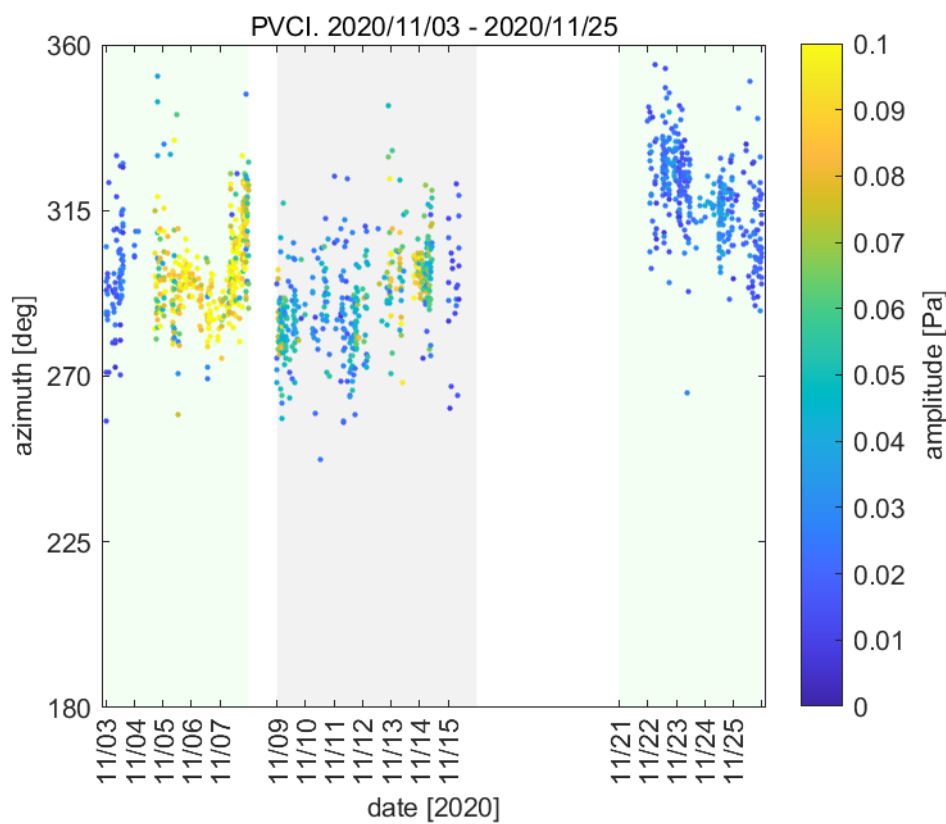
316 in the plot represents one detection family. Green background marks the streamer events, grey
317 background marks the calm period.

318

319 PPCI detects arrivals from the north-west as well (Figure 4). Fluctuating signal
320 amplitudes are observed. Values around 0.02 Pa occur on 3 November. From 4th
321 November, 18 UTC to 7th November, 22:30 UTC, the signals are of amplitudes around
322 0.089 Pa. The amplitudes decrease to the values around 0.046 Pa during the consequent
323 quiet period and further to 0.024 Pa during the streamer on 21st – 25th November. Trace
324 velocities are similar during streamers and quiet periods. The velocities fluctuate between
325 0.335 and 0.494 km·s⁻¹; no significant signatures of the streamers are identified in the signal
326 trace velocity.

327 The observations at WBCI and PPCI from 3rd to 25th November 2020 can be summarized
328 as follows. During the streamer event, the decrease in signal frequency is observed at
329 WBCI. At PPCI, the increased signal amplitudes occur. Signal trace velocities seem
330 uninfluenced by the streamers.

331



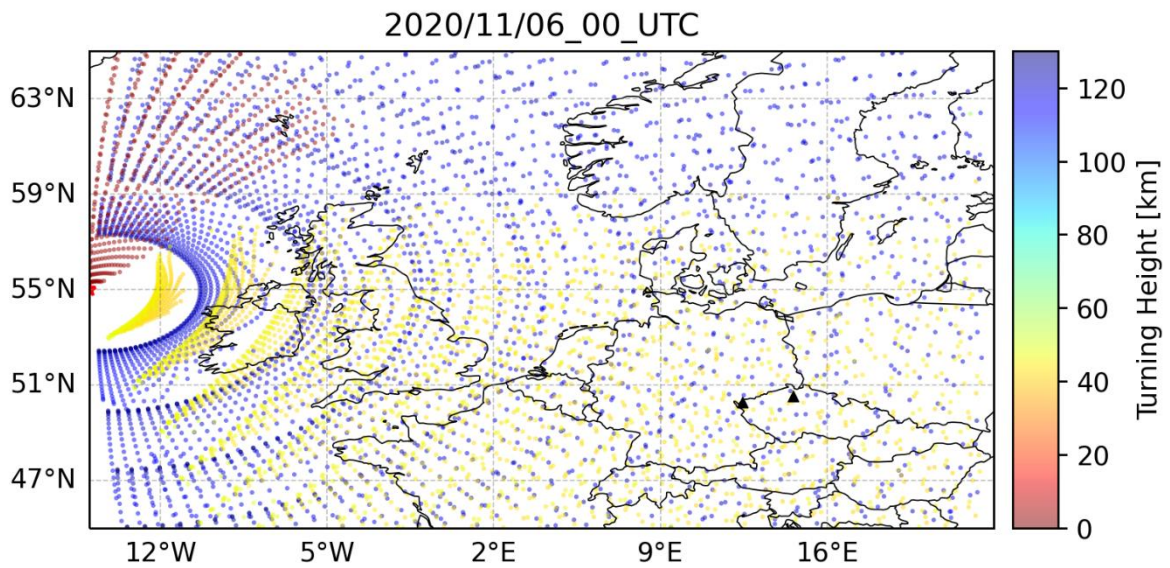
333 Fig.4. Infrasound observations at PPCI on 3rd - 25th November 2020. Azimuth of signal
334 arrival is shown; the colorbar refers to the signal amplitude. Green background marks the
335 streamer events, grey background marks the calm period.

336

337 To approximate propagation of signals from a source located at the surface of the North
338 Atlantic, the InfraGA/GeoAc tools are employed. Propagation of the 0.2 Hz signals is
339 modelled on 6th November at 00 UTC. Three scenarios represent propagation conditions
340 influenced by a streamer event. The fictitious point sources are located (1) at 55°N and
341 15°W, (2) at 55°N and 5°W, and (3) at 60°N and 0° longitude. The coordinates of the
342 sources are estimated based on the position of the tropopause jet stream disturbance. Taking
343 into account the mutual locations of the sources and the receiving arrays, eastward signal
344 propagation is modelled. The azimuth limits are set to 0° and 180°, the azimuth step is 3°.
345 Signal inclinations 2° – 45° are considered in 2° resolution. As a reference, signal
346 propagation from a source at 55°N and 15°W is modelled on the calm day, 12th November
347 at 00 UTC.

348 Stratospheric arrivals are expected by the model in Central Europe from the sources at the
349 latitude of 55°N during the streamer event as well as on the calm day. Signal propagation
350 through the thermospheric waveguide is possible from all the considered sources during the
351 streamer event and on the calm day (Figures 5 – 8). The decrease of signal frequency
352 observed at WBCI on 5th – 6th November from 20 to 05 UTC can indicate that
353 thermospheric ducting transiently prevailed over the stratospheric waveguide.

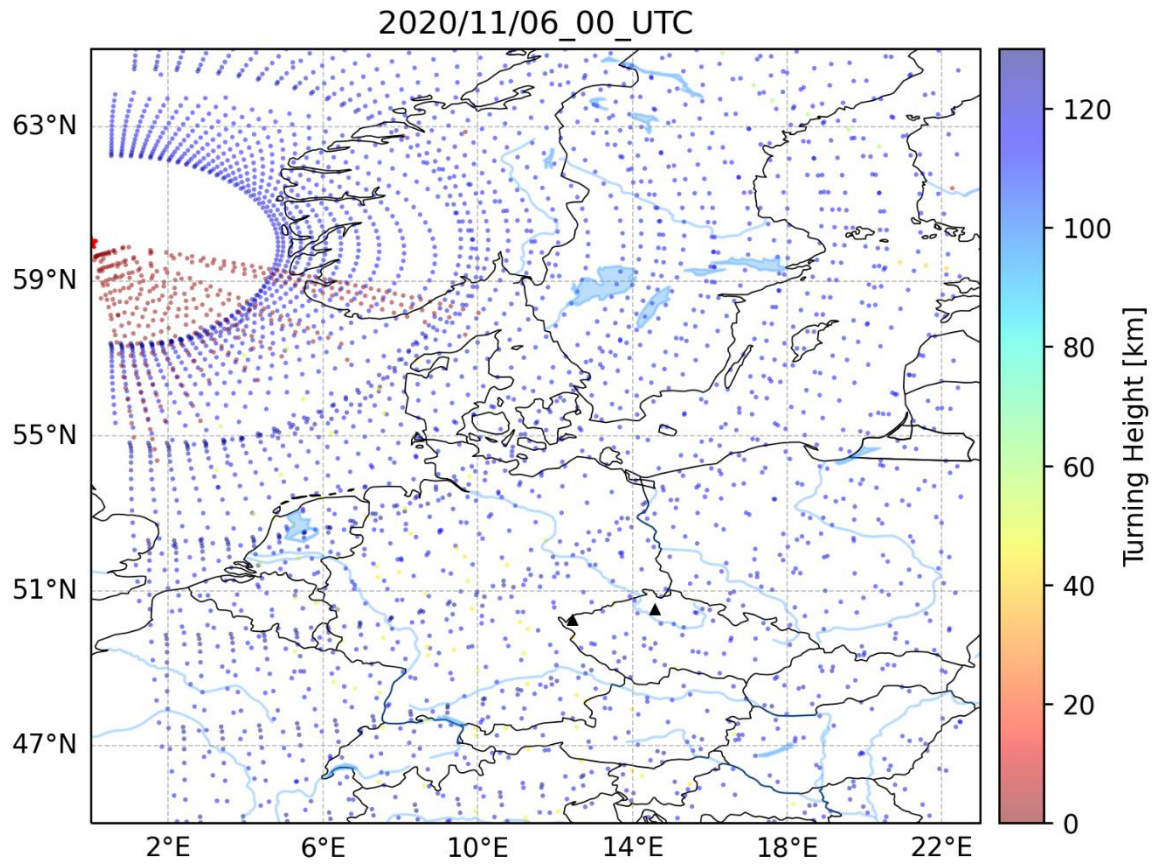
354



355

356 Fig.5. Model of infrasound propagation from a point source located at 55°N and 15°W (red
 357 asterisk) during the streamer event on 6th November 2020 at 00 UTC. Colobar refers to the
 358 turning heights of the signal. Red indicates signal propagation in the waveguide formed near
 359 the tropopause (altitudes around 10 km), arrivals through the stratospheric waveguide are in
 360 yellow (altitudes around 40-50 km) and arrivals through the thermospheric waveguide are in
 361 blue (altitudes above 100 km). Black triangles represent infrasound arrays WBCI (the left
 362 triangle) and PVICI (the right triangle).

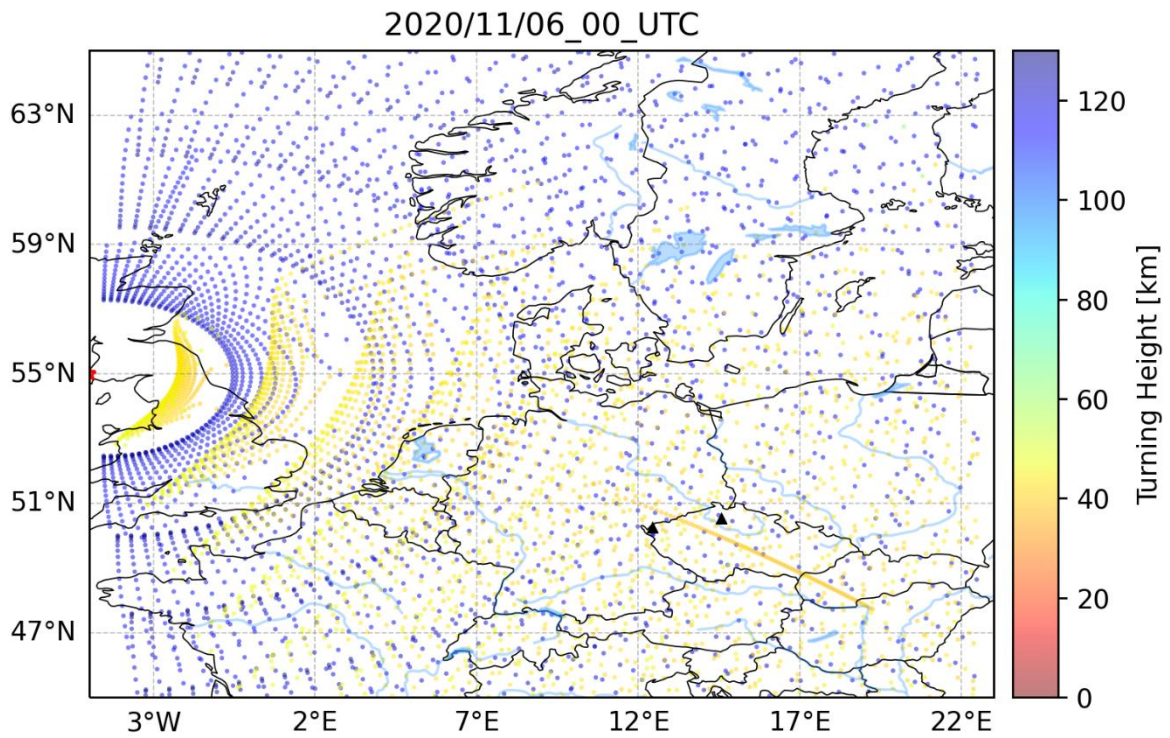
363



364

365 Fig.6. The same as Figure 5, but for the source located at 60°N 0°longitude. The stratospheric
 366 waveguide is not significantly involved in infrasound ducting to Central Europe.

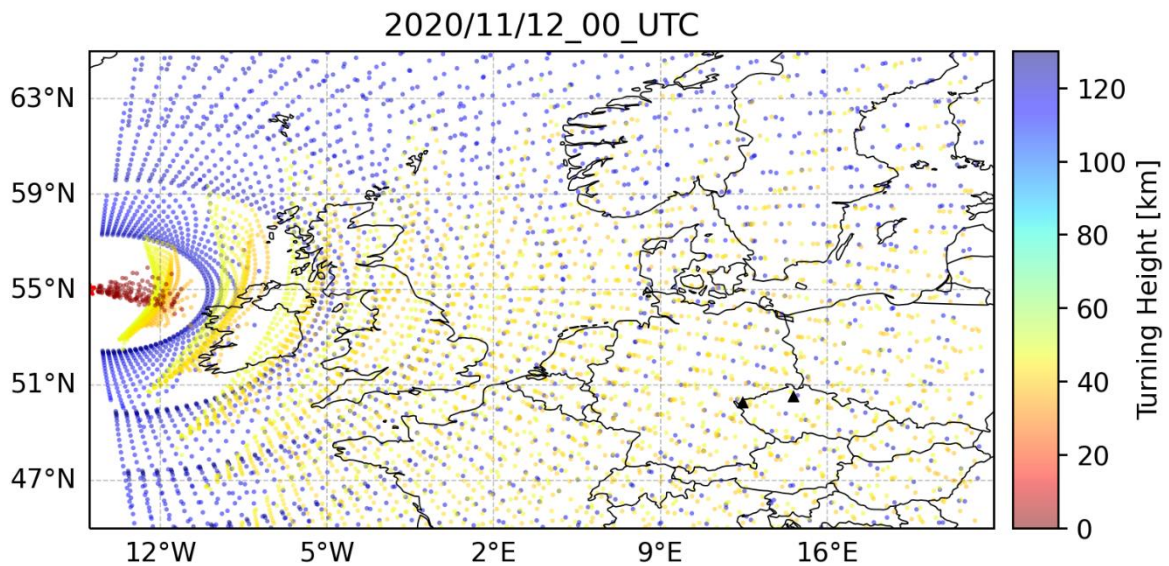
367



368

369 Fig.7. The same as Figure 5, but for the source located at 55°N 5°W. The tropospheric
 370 waveguide does not influence propagation to the East of the source.

371



372
 373 Fig.8. Model of infrasound propagation from a point source located at 55°N and 15°W (red
 374 asterisk) on the quiet day of 12th November 2020 at 00 UTC. The meaning of the symbols and
 375 colours is the same as in Figure 5.

376
 377 It follows from Figures 5 – 7, that the effects of the streamer event occur in the limited
 378 regions close to the sources. Northward propagating signals from a source at 55°N and
 379 15°W are guided by the northward jet-stream above the source location (Figure 5). Signals
 380 from the source at 60°N 0°longitude propagate in the opposite direction; southward
 381 waveguide at the tropopause is formed by the southward jet-stream near the west coast of
 382 southern Scandinavia (Figure 6). Tropospheric – tropopause ducting is not predicted for
 383 signals emitted by the source located between the northward and southward branch of the
 384 jet-stream wave (Figure 7). It follows from the InfraGA/GeoAc outputs that signal
 385 propagation from sources in the North Atlantic to Central Europe is not significantly
 386 modified by the streamer event on 6th November 2020 at 00 UTC.

387 Publicly available data – meteorological charts provided by Deutscher Wetterdienst and
 388 the WAVEWATCHIII[®] wave-action model (The WAVEWATCHIII[®] Development Group,
 389 2016) indicate that there was a maritime storm in progress in the North Atlantic within the

390 time window of the first streamer. The storm could cause intensification of the microbarom
391 source and as a consequence, increased signal amplitudes were observed at PPCI on 4th –
392 7th November.

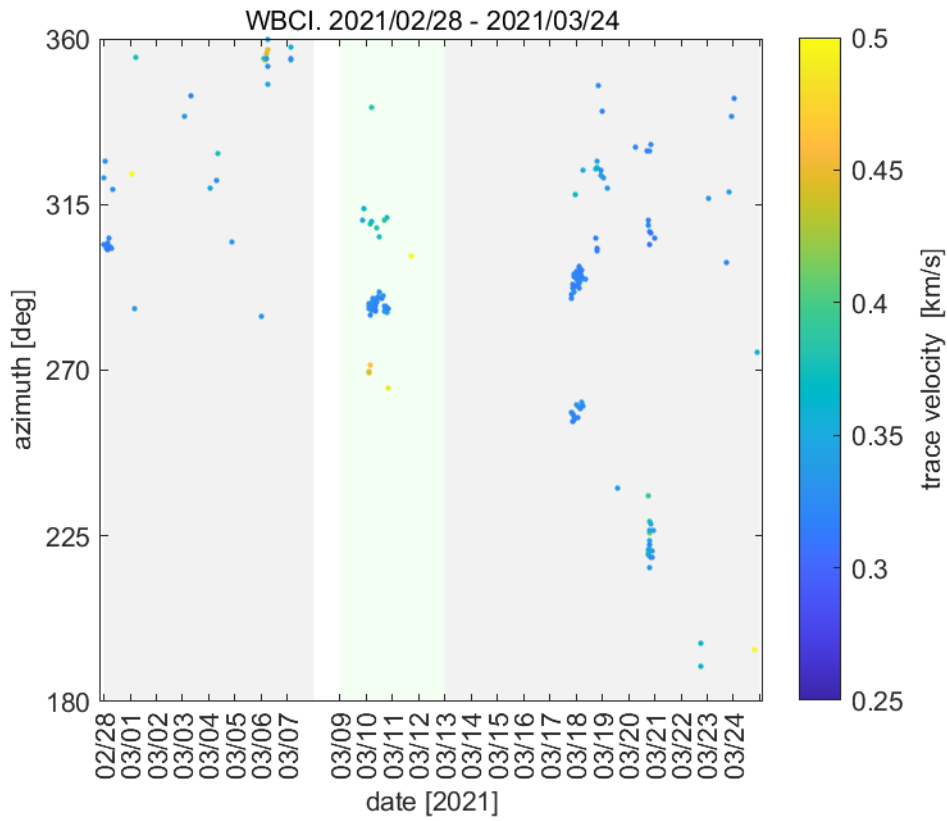
393

394 **3.1.2 Infrasound observations from 28th February to 24th March 2021**

395 A streamer event occurred from 9th to 12th March 2021 preceded and followed by calm
396 periods from 28th February to 7th March and from 13th to 24th March, respectively.

397 Both WBCI and PPCI detect signals arriving from the north-west, from back-azimuths of
398 285° – 310°. An increase of signal trace velocities is observed in some of the detections at
399 WBCI during the streamer event compared to calm periods (Figure 9). Trace velocities of
400 0.460 km/s and 0.380 km/s are observed from back-azimuths of 270° and 310° on 10th March
401 at 00 – 06 UTC, respectively. It is by 0.05 – 0.13 km/s higher than on the calm days.
402 Contrary, PPCI records a decrease in trace velocities on 10th March at 00 – 06 UTC (Figure
403 10). Trace velocities of 0.377 km/s are observed compared to 0.413 km/s and 0.395 km/s
404 during the calm periods before and after the streamer, respectively. Differences between the
405 streamer event and calm periods are not observed in signal amplitudes and frequencies. Mean
406 signal frequencies remain around 0.2 Hz and amplitudes vary between 0.003 and 0.049 Pa
407 without any trend.

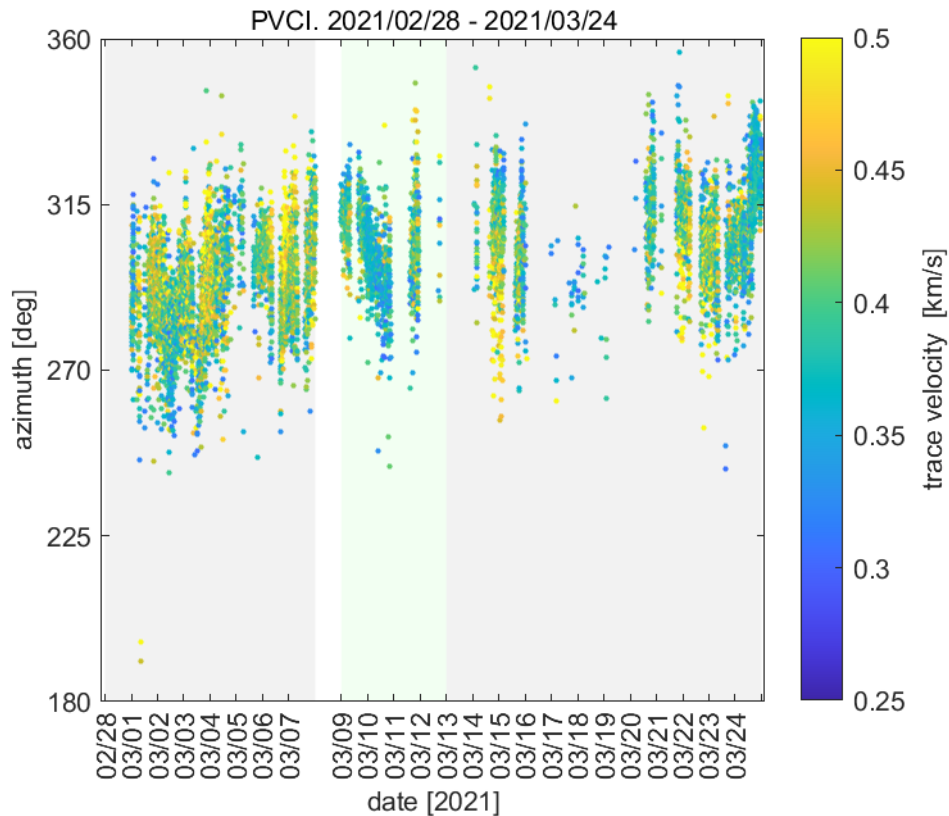
408



409

410 Fig.9. Infrasound observations at WBCI on 28th February – 24th March 2021. Azimuth of
 411 signal arrival is shown; the colorbar refers to the signal trace velocity. Green background
 412 marks the streamer event, grey background marks the calm periods.

413



414

415 Fig.10. Infrasound observations at PPCI on 28th February – 24th March 2021. Azimuth of
 416 signal arrival is shown; the colorbar refers to the signal trace velocity. Green background
 417 marks the streamer event, grey background marks the calm periods.

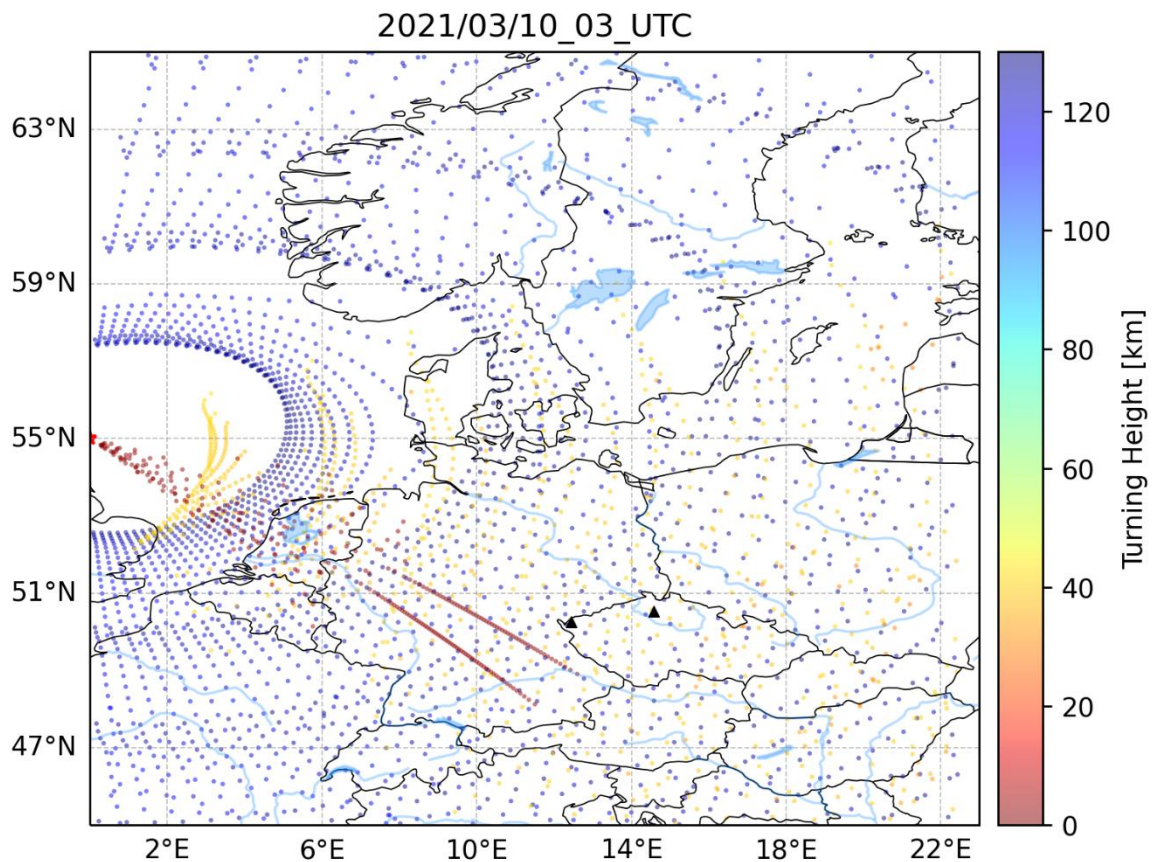
418

419 The different trace velocities observed during the streamer event and during the calm
 420 periods can indicate modifications of the atmospheric waveguides. The theoretical
 421 relationship between the signal trace velocity and celerity presented by Lonzaga (2015)
 422 relates lower trace velocities to signals refracted at lower altitudes. The exact limits of the
 423 trace velocity for the given atmospheric waveguide depend on the current state of the
 424 atmosphere. The decrease of the trace velocities observed at PPCI can indicate transient
 425 signal propagation in the tropospheric waveguide. Increased trace velocities at WBCI can
 426 be explained as arrivals from the upper atmospheric regions. However, effects of spatial
 427 aliasing must also be taken into account at the WBCI detections, especially considering that
 428 the signal frequencies are around 0.2 Hz, well above the range of array optimum
 429 performance. The observed increase of trace velocities at WBCI can therefore be a
 430 processing bias rather than a consequence of signal refraction at higher altitudes.

431 Like in the November 2020 case, we employ the InfraGA/GeoAc tools to investigate
 432 infrasound propagation paths on 10th March at 03 UTC. Propagation of the 0.2 Hz signal is

433 modelled. A source is located at 55°N 15°W; this scenario represents signal propagation
434 from the central North Atlantic. The other source is located at 55°N 0°latitude representing
435 propagation of microbaroms from the North Sea. Propagation in azimuths 0° – 180° of the
436 source is studied. For both sources, InfraGA/GeoAc predicts eastward signal propagation in
437 the stratospheric and thermospheric waveguides. The other eastward waveguide occurs near
438 the tropopause, formed by the eastward to south-eastward jet-stream above the eastern
439 North Atlantic and Western Europe at latitudes 50 – 60°N. Signals emitted by a source in
440 the North Sea are expected to propagate also through this waveguide to Central Europe
441 (Figure 11). Though the simulation of signal propagation from a point source is an
442 approximation of the real situation – microbaroms are emitted by a source that is
443 considered planar, the model results suggest that the fluctuations of microbarom trace
444 velocity observed at PPCI on 10th March 2021 can be influenced by the tropospheric
445 waveguide. Tropospheric waveguides in general are considered less stable compared to the
446 waveguides in the middle and upper atmosphere (Drob et al., 2003).

447



448

449 Fig.11 Model of infrasound propagation from a point source located at 55°N and 0°longitude
450 (red asterisk) on 10th March 2021 at 03 UTC. The waveguide near the tropopause is expected
451 to influence infrasound propagation to Central Europe.

452

453

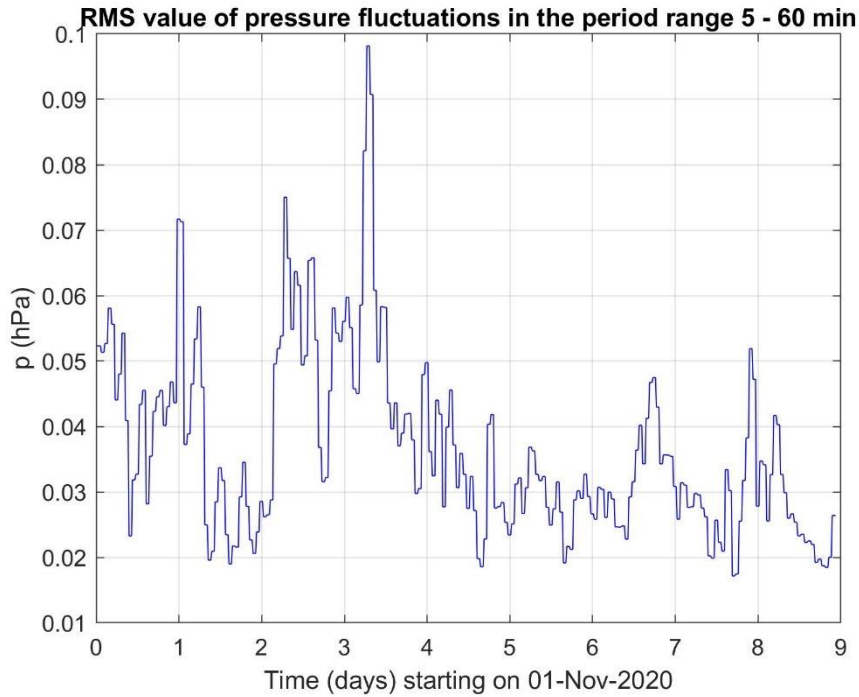
454 **3.2 Results and discussion of gravity waves in the troposphere and ionosphere**

455

456 **3.2.1 Investigation of GWs measured on the ground by WBCI array of micro-** 457 **barometers.**

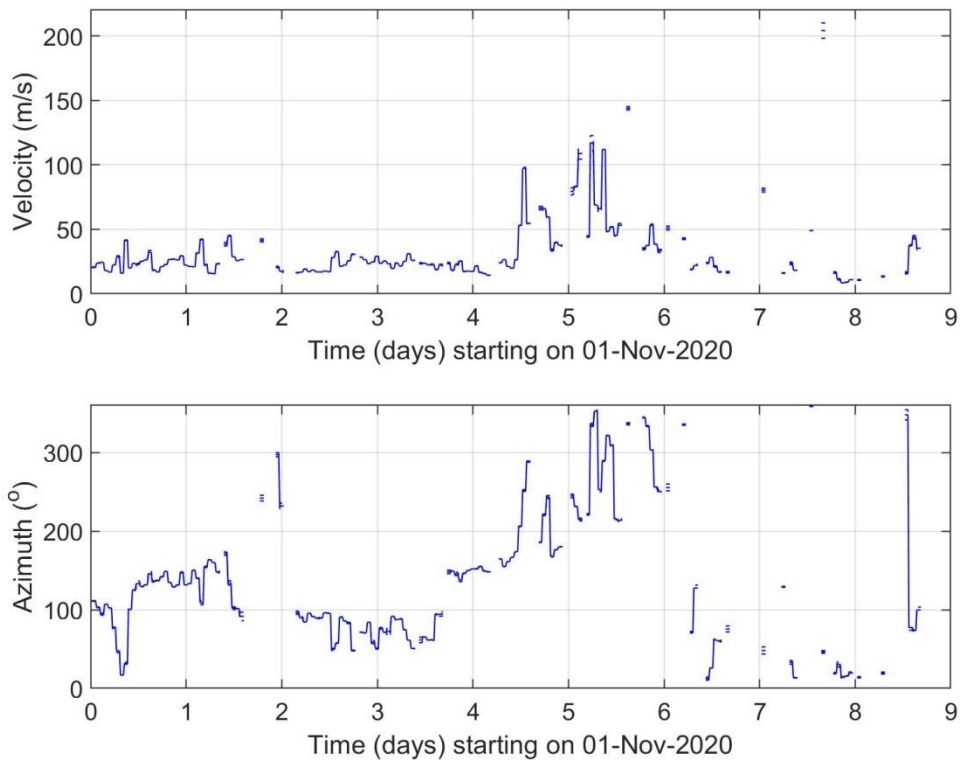
458 . Figure 12 shows the RMS amplitudes of pressure fluctuations in the period range 5-60 min
459 recorded from November 1 to November 9, 2020. This interval covers a distinct streamer
460 event that occurred from November 3 to November 7. The results of propagation analysis are
461 shown in Figure 13, which displays the phase velocities and azimuths of GWs. Only results
462 that satisfied the criterion ($dv/v < 0.5$) and ($dAZ < 10^\circ$) and ($p_{RMS} > 0.02$ Pa) are presented,
463 where dv/v , dAZ , p_{RMS} are the relative uncertainty of GW phase velocity, uncertainty of
464 azimuth and root mean square value of pressure fluctuations in the analysed time interval.
465 Figure 13 demonstrates that there is a tendency for higher phase velocities and occurrence of
466 different azimuths during the streamer event. Therefore, it is useful to compare the GW
467 characteristics during streamer events and calm conditions.

468 Figure 14 shows histograms obtained by a statistical analysis. The RMS amplitudes of
469 pressure fluctuations in the period range 5 – 60 min, phase velocities and azimuths were
470 investigated separately for calm conditions (upper plots) and for streamer events listed in
471 Table 1 (bottom plots) with a 1-hour time resolution. The solid vertical lines mark lower (Q1)
472 and upper (Q3) quartiles. The dashed vertical lines depict boundaries for large ($Q3 + 1.5 \cdot (Q3 -$
473 $Q1)$) and extreme ($Q3 + 3 \cdot (Q3 - Q1)$) values. A difference between histograms for RMS
474 pressure fluctuations and azimuths obtained for calm and disturbed conditions is obvious. A
475 minor difference is also observed for phase velocities.



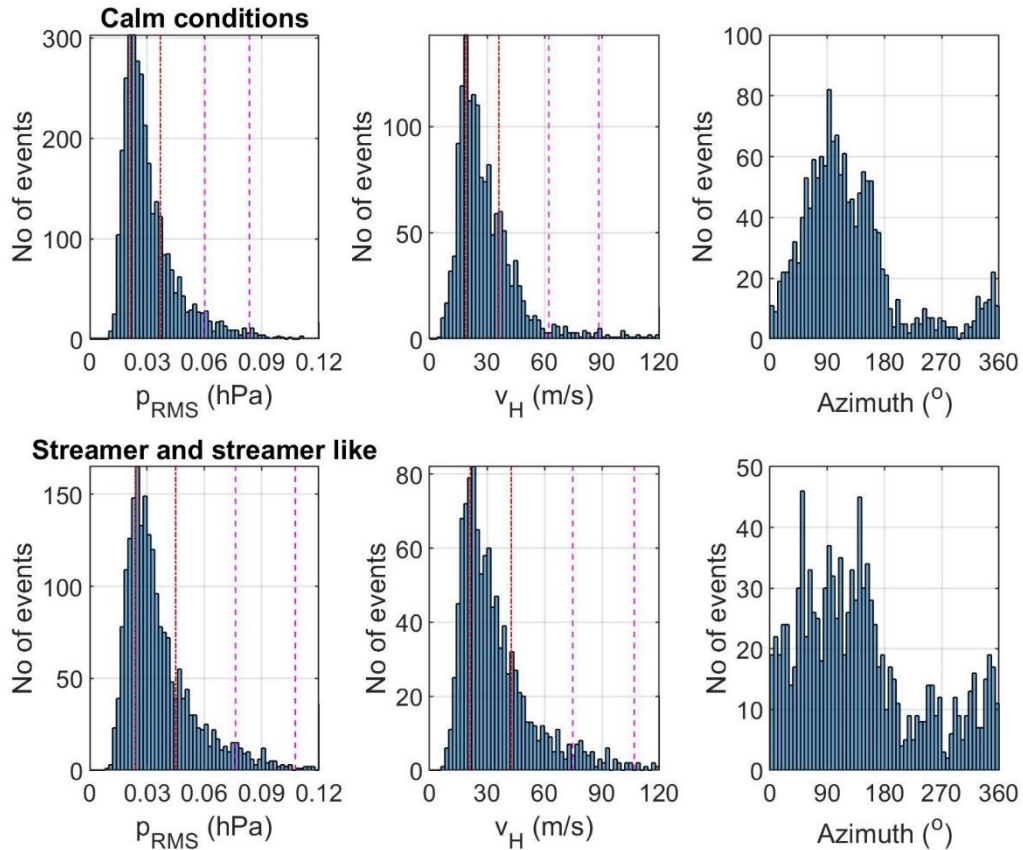
476

477 **Figure 12** Amplitude of GWs recorded by WBCI from 2020-11-01 to 2020-11-09



478

479 **Figure 13** Propagation velocity and azimuth of GWs recorded by WBCI from 2020-11-01 to
 480 2020-11-09



481

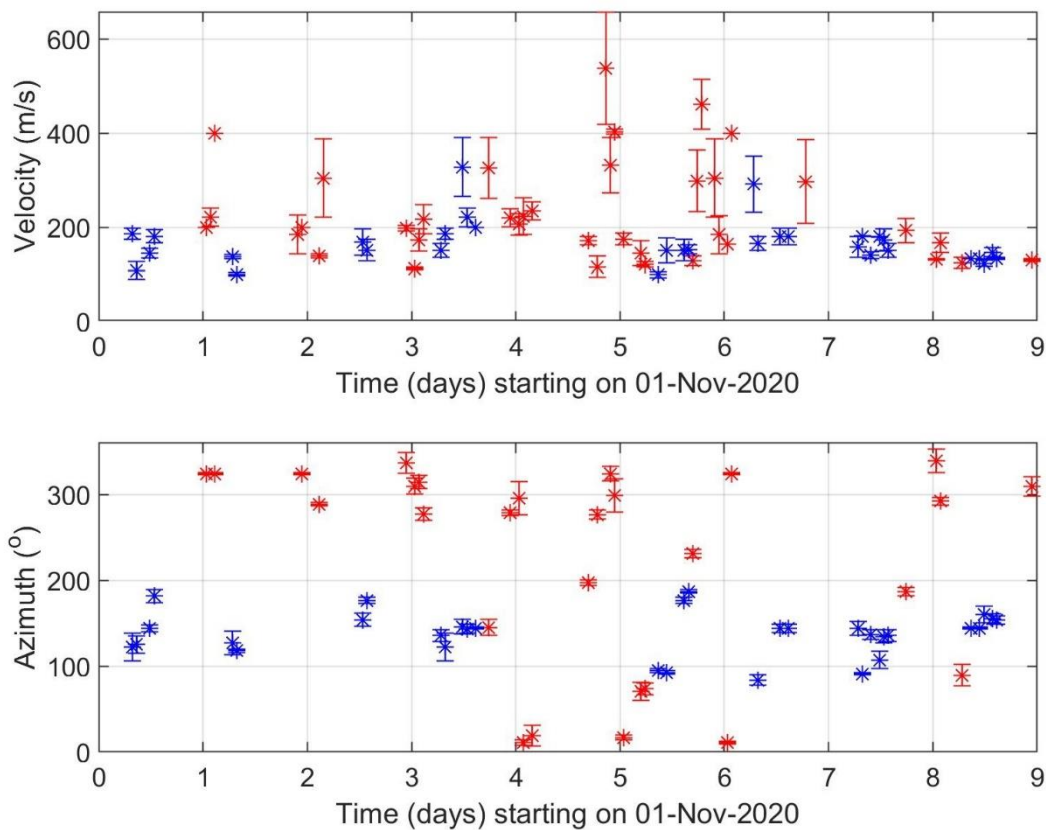
482 **Figure 14** GW characteristics (RMS of pressure fluctuations, phase velocity and azimuth)
 483 for calm periods (upper plots) and streamer and streamer like events (bottom plots) for 2020
 484 and winter 2021. The red vertical lines mark lower (Q1) and upper (Q3) quartiles. The dashed
 485 magenta vertical lines depict boundaries for large ($Q3 + 1.5 \cdot (Q3 - Q1)$) and extreme ($Q3 + 3 \cdot (Q3 -$
 486 $Q1)$) values.

487

488 3.2.2 Investigation of GWs measured in the ionosphere by continuous Doppler 489 sounding system (CDS)

490 The 2D propagation analysis of GWs was performed using the 2D versions of methods
 491 mentioned in Section 2 and in detail described by Chum and Podolská (2018). As discussed in
 492 Section 2 and by (Chum et al., 2021), the 2D propagation analysis makes it possible to
 493 analyze much larger number of time intervals than the 3D analysis. The propagation analysis
 494 obtained for the interval from 1st November to 9th November 2020, which covers the
 495 significant streamer event that occurred from 3rd November 2020 to 7th November 2020, is
 496 presented in Figure 15. Only results that satisfied the criteria ($dv/v < 0.2$) and ($dAZ < 20^\circ$) and

497 ($f_{\text{DRMS}} > 0.05$ Hz) and ($C_{\text{max}} < 0.5$) are presented, where dv/v is the relative uncertainty of GW
 498 phase velocity, dAZ is the azimuth uncertainty, f_{DRMS} is the root mean square of the Doppler
 499 shift in the analysed time interval and C_{max} is the maximum in the normalized energy map for
 500 the best beam (slowness) search; C_{max} is 1 for identical signals (Chum and Podolská, 2018). It
 501 is considered that signals are not sufficiently correlated (coherent) for reliable propagation
 502 analysis if $C_{\text{max}} < 0.5$ (Chum et al., 2021). The velocities and azimuth obtained by observation
 503 at 3.59 MHz are in red, whereas the values based on measurements at 4.65 MHz are in blue.
 504 Obviously, the observations at 3.59 MHz mostly correspond to the nighttime, whereas
 505 observations at 4.65 MHz were mostly made during the daytime. **The 4.65 MHz signal did not**
 506 **reflect from the ionosphere (escaped to the outer space) at night due to the low critical**
 507 **frequency of the ionosphere. On the other hand, the 3.59 MHz signal mostly reflected during**
 508 **the day from the ionospheric E layer and the Doppler shift was negligible, difficult to**
 509 **analyse**. The GWs usually propagated roughly poleward at night and roughly equatorward
 510 during the daytime. This is fully consistent with the statistical investigation (Chum et al.,
 511 2021) which showed that propagation directions of GWs in the ionosphere exhibit diurnal and
 512 seasonal behaviour and are mainly controlled by the neutral winds in the thermosphere.



513

514 **Figure 15** Propagation velocity and azimuth of GWs in the ionosphere obtained using CDS
515 measurements from 2020-11-01 to 2020-11-09. The velocities and azimuth obtained by
516 observation at 3.59 MHz are by red, whereas the values based on measurements at 4.65 MHz
517 are by blue.

518 Based on the analysis of the GW observed in the ionosphere during the streamer event and
519 on the previous statistical analysis, we conclude that no obvious signature related to streamer
520 event was observed for the propagation of GW the ionosphere.

521 It should be also mentioned that the phase velocities of GW measured on the ground (Figure
522 8) and at heights around 200 km in the ionosphere differ. There are several reasons for that.
523 First, the observed horizontal phase velocities depend on the elevation angle of GW
524 propagation and on the ambient temperature as follows from the dispersion relation (the
525 temperature enters the dispersion relation via the buoyancy frequency and the scale height).
526 The temperature in the ionosphere/thermosphere is several times higher than in the
527 troposphere. The elevation angles might change during the upward propagation of GWs,
528 depending on the wind and temperature profile. Second, GWs propagate with a tilt, not
529 vertically upward. It is therefore highly probable that the sources of the GWs observed in the
530 troposphere and ionosphere are different. Moreover, GW can break during their propagation
531 upward and secondary gravity waves might be observed in the ionosphere.

532 **4) Conclusion and discussion**

533 The focus of this study was to test independent types of observations like Doppler sounding
534 and microbarograph measurements for an analysis of GW behavior during streamer events,
535 which are strongly connected with PW or GW and the large scale mass transport of ozone and
536 that is why it can be very interesting for studies of atmospheric dynamics.

537 The other aim of the study was to find phenomena in infrasound arrival parameters that
538 could serve as a quick indicator of streamers and that could be identified during the routine
539 processing of infrasound detections. Infrasound observations at two Central European
540 stations PPCI and WBCI were studied; signal propagation through a range dependent
541 atmosphere was modelled using the InfraGA/GeoAc tools. In November 2020 and in
542 March 2021, the dynamics of the tropopause – lower stratosphere region was influenced by
543 streamer events. During the streamer in November 2020, a transient decrease of signal
544 frequency was observed at WBCI; at PPCI signal amplitudes varied. Streamer-related
545 signatures were observed in trace velocities at neither of the stations. Contrary in March

546 2021, fluctuations of signal trace velocities occurred; the other signal arrival parameters
547 were not influenced by the streamer. Amplitude fluctuations at PPCI in November 2020
548 were likely related to a variable intensity of the microbarom source caused by a maritime
549 storm. The variations of trace velocities in March 2021, particularly at PPCI can be
550 attributed to the waveguide which developed at the tropopause and which influenced
551 signals propagating from the North Sea to Central Europe. In November 2020, signal
552 propagation from the North Atlantic to Central Europe was not modified by the streamer.
553 Signal propagation in the stratospheric and thermospheric waveguide was expected during
554 the streamer event; similar propagation conditions occurred on the calm day. Since both
555 waveguides were involved in infrasound ducting, it was possible that WPCI transiently
556 detected signals travelling in the thermospheric waveguide and as a consequence decrease
557 of signal frequencies was observed.

558 Streamer events are dynamical phenomena. Their exact occurrence location as well as their
559 impact on the tropopause – lower stratosphere region differs from event to event. It is
560 therefore tricky to identify typical signatures of streamers in infrasound measurements that
561 could serve as a reliable indicator of streamers.

562 Supplementary ground-based measurements of GW using the WPCI array in the
563 troposphere showed that GW propagation azimuths were more random during streamer and
564 streamer-like events compared to those observed during calm conditions. At the same time,
565 larger GW amplitudes were observed in the troposphere during streamer and streamer-like
566 events than under quiescent conditions. On the other hand, the GW propagation
567 characteristics observed in the ionosphere by CDS during streamer events did not differ from
568 those expected for the given time period, based on previous statistical studies (Chum et al.,
569 2021).

570 The results therefore indicate that streamers in the stratosphere might lead to changes in wave
571 propagation in the troposphere. The impact on the ionosphere was not confirmed, but cannot
572 be excluded due to sparse and localized observations of GW activity. In general, to validate the
573 preliminary results obtained in this study, a denser measurement network and more streamer
574 events need to be analyzed.

575 **Data availability:**

576 ozone column measurements (TO3) which are available as a service by DLR at
577 <https://atmos.eoc.dlr.de/>

578 Ground to space model vertical atmospheric profiles were obtained at
579 <https://g2s.ncpa.olemiss.edu/>; accessed on 27 January – 4 February 2024

580

581 The WAVEWATCHIII[®] wave-action model data were accessed via ftp at
582 [polar.ncep.noaa.gov/waves/JCOMM/2020](ftp://polar.ncep.noaa.gov/waves/JCOMM/2020) on 13-14 March 2023.

583

584 The Deutscher Wetterdienst synoptic charts were accessed at
585 https://www2.wetter3.de/archiv_dwd_dt.html on 3 February 2024.

586

587 **Author contributions**

588 MK and LK create the idea of manuscript; JCh, MK, TS, LK, and KP suggest the datasets and
589 methods; TS, JCh, LK, KP and FT analyzed the data; MK wrote the manuscript draft; JCh,
590 TS, LK and KP reviewed and edited the manuscript.

591 **Competing interests**

592 The authors declare that they have no conflict of interest.

593

594 **Acknowledgement**

595 The DTK-GPMCC software was kindly provided by Commissariat à l'énergie atomique et
596 aux énergies alternatives, Centre DAM-Île-de-France, Département Analyse, Surveillance,
597 Environnement, Bruyères-le-Châtel, F91297 Arpajon, France.

598 The authors are grateful to Dr. Phil Blom and Los Alamos National Laboratory for opening
599 the InfraGA/GeoAc tools to the public.

600 **Financial support:** This study is supported by LISA project- Lidar measurements to
601 Identify Streamers and analyze Atmospheric waves, AEOLUS-INNOVATION, Contract No.
602 4000133567/20/I-BG

603

604 **References**

605 Assink, J.D., Waxler, R., Smets, P., Evers, L.G. (2014). Bidirectional infrasonic ducts
606 associated with sudden stratospheric warm-ing events. *J. Geophys. Res. Atmos.* 119,1140-
607 1153.

608 Bittner, M., Höppner, K., Pilger, C., Schmidt, C. (2010). Mesopause temperature
609 perturbations caused by infrasonic waves as a potential indicator for the detection of
610 tsunamis and other geo-hazards. *Nat. Hazards Earth Syst. Sci.*, 10, 1431-1442. [www.nat-](http://www.nat-hazards-earth-syst-sci.net/10/1431/2010/doi:10.5194/nhess-10-1431-2010)
611 [hazards-earth-syst-sci.net/10/1431/2010/doi:10.5194/nhess-10-1431-2010](http://www.nat-hazards-earth-syst-sci.net/10/1431/2010/doi:10.5194/nhess-10-1431-2010)

612 Blanc, E. (1985). Observations in the upper atmosphere of infrasonic waves from natural or
613 artificial sources: A summary. *Ann. Geophys.*, 3, 673-688.

614 Blixt, E.M., Nasholm, S.P., Gibbons, S.J., Evers, L.G., Charlton-Perez, A.J., Orsolini, Y.J.,
615 Kvaerna, T. (2019). Estimating tropo-spheric and stratospheric winds using infrasound from
616 explosions. *J. Acoust. Soc. Am.* 146:2.

617 Blom, P., Waxler, R. (2012). “Impulse propagation in the nocturnal boundary layer: Analysis
618 of the geometric component”. *J. Acoust. Soc. Am.*, **131**, 3680 – 3690. doi:
619 [10.1121/1.3699174](https://doi.org/10.1121/1.3699174).

620 Blom, P. (2019). “Modeling infrasonic propagation through a spherical atmospheric layer:
621 Analysis of the stratospheric pair.” *J. Acoust. Soc. Am.*, **145**, 2198–2208. doi:
622 [10.1121/1.5096855](https://doi.org/10.1121/1.5096855).

623 Bondár I., T. Šindelářová, D. Ghica, U. Mitterbauer, A.Liashchuk, J. Baše, J. Chum, C.
624 Czanik, C. Ionescu, C. Neagoe, M. Pásztor, A. Le Pichon (2022), Central and Eastern
625 European Infrasound Network: Contribution to Infrasound Monitoring, *Geophys. J. Int.*,
626 ggac066, <https://doi.org/10.1093/gji/ggac066>

627 Brachet, N., Brown, D., Le Bras R., Cansi, Y., Mialle, P., Coyne, J. (2010). Monitoring the
628 Earth’s Atmosphere with the Global IMS Infrasound Network. In: Le Pichon, A., Blanc, E.,
629 Hauchecorne A. (Eds.), *Infrasound Monitoring for Atmospheric Studies*. Springer
630 Science+Business Media B.V., 77-118. Doi: 10.1007/978-1-4020-9508-5_3

631 Campus, P., Christie, D.R. (2010). Worldwide Observations of Infrasonic Waves. In: Le
632 Pichon, A., Blanc, E., Hauchecorne A. (Eds.), *Infrasound Monitoring for Atmospheric*
633 *Studies*. Springer Science+Business Media B.V., 185234-118. Doi: 10.1007/978-1-4020-
634 9508-5_6

635 Cansi, Y., 1995. An automatic seismic event processing for detection and location: The
636 P.M.C.C. method. *Geophys. Res. Lett.* 22, 1021-1024. doi: 10.1029/95GL00468

637 Ceranna, L., Matoza, R., Hupe, P., Le Pichon, A., Landès, M., (2019). Systematic Array
638 Processing of a Decade of Global IMS Infrasound Data. In: Le Pichon, A., Blanc, E.,
639 Hauchecorne, A. (eds) Infrasound Monitoring for Atmospheric Studies. Chal-lenges in
640 Middle Atmospheric Dynamics and Societal Benefits. Springer Nature Switzerland AG.

641 Chum J, Podolská K (2018) 3D analysis of GW propagation in the ionosphere. Geophysical
642 Research Letters, 45, 11,562–11,571, <https://doi.org/10.1029/2018GL07969>

643 Chum, J., Podolská, K., Rusz, J., Baše, J., Tedoradze, N. (2021), Statistical investigation of
644 gravity wave characteristics in the ionosphere. Earth Planets Space 73, 60,
645 <https://doi.org/10.1186/s40623-021-01379-3>

646 **Czech microbarograph network**, <https://doi.org/10.7914/SN/C9>

647 Drob, D. P., Picone, J. M., Garcés, M. (2003). Global morphology of infrasound propagation.
648 *J. Geophys. Res. Atmospheres*, **108** (D21). doi: [10.1029/2002JD003307](https://doi.org/10.1029/2002JD003307).

649 Evers, L. G., Siegmund, P. (2009). Infrasonic signature of the 2009 major sudden
650 stratosphericwarming, *Geophys. Res. Lett.*, 36, L23808, doi:10.1029/2009GL041323

651 Evers, L.G., Haak, H.W. (2010). The Characteristics of Infrasound, its Propagation and Some
652 Early History. In: Le Pichon, A., Blanc, E., Hauchecorne, A. (eds) Infrasound Monitoring for
653 Atmospheric Studies. Springer, Dordrecht.

654 Evers, L. G., van Geyt, A. R. J. , Smets, P., Fricke, J.T. (2012). Anomalous infrasound
655 propagation in a hot stratosphere and the existence of extremely small shadow zones, *J.*
656 *Geophys. Res.*, 117, D06120, doi:10.1029/2011JD017014.

657

658 Eyring, V., Dameris, M., Grewe, V., Langbein, I., & Kouker, W. (2002). Climatologies of
659 streamer events derived from a transport model and a coupled chemistry-climate model.

660 Fritts, D.C. & Alexander, M.J., (2003). Gravity wave dynamics and effects in the middle
661 atmosphere. *Rev. Geophys.*, 41 (1), 1003.

662 Garcès, M., Willis, M., Hetzer, C., Le Pichon , A., Drob, D., (2004). On using ocean swells
663 for continuous infrasonic measurements of winds and temperature in the lower, middle, and
664 upper atmosphere. *Geophys. Res. Lett.* 31, L19304. doi: 10.1029/2004GL020696

665 Garcès, M.A., (2013). On infrasound standards, part 1: Time, frequency, and energy scaling.
666 *InfraMatics* 2, 13-35. doi: 10.4236/inframatics.2013.22002

667 Georges, T.M. (1968). H. F. Doppler studies of travelling ionospheric disturbances. *J.*
668 *Atmos.Terr. Phys.*, 30, 735-746.

669 Gerlach, C., Földvary, L., Švehla, D., Gruber, T., Wermuth, M., Sneeuw, N., ... &
670 Steigenberger, P. (2003). A CHAMP-only gravity field model from kinematic orbits using the
671 energy integral. *Geophysical Research Letters*, 30(20).

672 Hersbach, H., Bell, B., Berrisford, P., Hirahara, S., Horányi, A., Muñoz-Sabater, J., ... &
673 Thépaut, J. N. (2020). The ERA5 global reanalysis. *Quarterly Journal of the Royal*
674 *Meteorological Society*, 146(730), 1999-2049.

675 Hupe, P., Ceranna, L., Pilger, C., de Carlo, M., Le Pichon, A., Kaifler, B., Rapp, M. (2019).
676 Assessing middle atmosphere weather models using infrasound detections from microbaroms.
677 *Geophys. J. Int.*, 216, 1761–1767 doi: 10.1093/gji/ggy520

678 James, P. M. (1998): A climatology of ozone mini-holes over the Northern Hemisphere.
679 *International Journal of Climatology: A Journal of the Royal Meteorological Society*, 18, 12:
680 12871303

681 Kramer, R, S. Wüst, and M. Bittner (2016). Investigation of gravity wave activity based on
682 operational radiosonde data from 13 years (1997-2009): Climatology and possible induced
683 variability, *Journal of Atmospheric and Solar-Terrestrial Physics* 140, 23–33;
684 <http://dx.doi.org/10.1016/j.jastp.2016.01.014>

685 Kramer, R., S. Wüst, C. Schmidt, and M. Bittner (2015). Gravity wave characteristics in the
686 middle atmosphere during the CESAR campaign at Palma de Mallorca in 2011/2012: Impact
687 of extratropical cyclones and cold fronts, *Journal of Atmospheric and Solar-Terrestrial*
688 *Physics* 128 (2015) 8–23, <http://dx.doi.org/10.1016/j.jastp.2015.03.001>

689 Kai Ming Huang, Shao Dong Zhang, Fan Yi, (2010). Reflection and transmission of
690 atmospheric gravity waves in a stably sheared horizontal wind field, *Journal of Geophysical*
691 *Research: Atmospheres*, 10.1029/2009JD012687, **115**, D16,

692 Landès, M., Ceranna, L., Le Pichon, A., & Matoza, R. S. (2012). Localization of microbarom
693 sources using the IMS infrasound network. *Journal of Geophysical Research:*
694 *Atmospheres*, 117(D6).

695 Le Pichon, A., Cansi, Y. (2003). PMCC for infrasound data processing. *InfraMatics* 02, 1-9.

696 Le Pichon, A., Blanc, E., (2005). Probing high-altitude winds using infrasound. *J. Geophys.*
697 *Res.*, 110, D20104. doi: 10.1029/2005JD006020

698 Le Pichon, A., Ceranna, L., Garcès, M., Drob, D., Millet, C., (2006). On using infrasound
699 from interacting ocean swells for global continuous measurements of winds and temperature
700 in the stratosphere. *J. Geophys. Res.*, 111, D11106. doi: 10.1029/2005JD006690

701 Le Pichon, A., Vergoz, J., Blanc, E., Guilbert, J., Ceranna, L., Evers, L., Brachet, N., (2009).
702 Assessing the performance of the International Monitoring System's infrasound network:
703 Geographical coverage and temporal variabilities. *J. Geophys. Res.* 114, D08112. doi:
704 10.1029/2008JD010907

705 Leovy, C. B., Sun, C. R., Hitchman, M. H., Remsberg, E. E., Russell III, J. M., Gordley, L.
706 L., ... & Lyjak, L. V. (1985). Transport of ozone in the middle stratosphere: Evidence for
707 planetary wave breaking. *Journal of Atmospheric Sciences*, 42(3), 230-244.

708 Lonzaga, J.B., (2015). A theoretical relation between the celerity and trace velocity of
709 infrasonic phases, *J. Acoust. Soc. Am.*, 138, EL242-EL247.
710 <http://dx.doi.org/10.1121/1.4929628>

711 Loyola D.G., Koukouli M.E., Valks P., Balis D.S., Hao N., van Roozendaal M., Spurr R.J.D.,
712 Zimmer W., Kiemle S., Lerot C., Lambert J.-C. (2011) The GOME-2 total column ozone
713 product: Retrieval algorithm and ground-based validation, *Journal of Geophysical Research*,
714 vol. 116, D07302, Wiley-Blackwell

715 Marty, J., (2019). The IMS Infrasound Network: Current Status and Technological
716 Developments, in: Le Pichon, A., Blanc, E., Hauchecorn, A. (Eds.), *Infrasound Monitoring*
717 *for Atmospheric Studies. Challenges in Middle Atmosphere Dynamics and Societal Benefits.*
718 Springer Nature Switzerland AG, pp. 3–62. doi:10.1007/978-3-319-75140-5_1

719 McIntyre, M. E., & Palmer, T. N. (1983). Breaking planetary waves in the stratosphere.
720 *Nature*, 305(5935), 593-600.

721 Munro, R., Eisinger, M., Anderson, C., Callies, J., Corpaccioli, E., Lang, R., ... & Albinana,
722 A. P. (2006, June). GOME-2 on MetOp. In Proc. of The 2006 EUMETSAT Meteorological
723 Satellite Conference, Helsinki, Finland (Vol. 1216, p. 48).

724 Munro, R., et al. (2016): The GOME-2 instrument on the Metop series of satellites:
725 instrument design, calibration, and level 1 data processing – an overview, *Atmos. Meas.*
726 *Tech.*, 9, 1279–1301, <https://doi.org/10.5194/amt-9-1279-2016>.

727 Peters, D., Hoffmann, P., & Alpers, M. (2003). On the appearance of inertia-gravity waves on
728 the north-easterly side of an anticyclone. *Meteorologische Zeitschrift*, 12(1), 25-35

729 Polvani, L. M., & Plumb, R. A. (1992). Rossby wave breaking, microbreaking, filamentation,
730 and secondary vortex formation: The dynamics of a perturbed vortex. *Journal of Atmospheric*
731 *Sciences*, 49(6), 462-476.

732 Pramitha, M., Venkat Ratnam, M., Taori, A., Krishna Murthy, B. V., Pallamraju, D., and
733 Vijaya Bhaskar Rao, S. (2015). Evidence for tropospheric wind shear excitation of high-
734 phase-speed gravity waves reaching the mesosphere using the ray-tracing technique, *Atmos.*
735 *Chem. Phys.*, 15, 2709–2721, <https://doi.org/10.5194/acp-15-2709-2015>.

736 Rauthe, M., Gerding, M., Höffner, J., & Lübken, F. J. (2006). Lidar temperature
737 measurements of gravity waves over Kühlungsborn (54° N) from 1 to 105 km: A winter-
738 summer comparison. *Journal of Geophysical Research: Atmospheres*, 111(D24).

739

740 Wüst, S., & Bittner, M. (2006). Non-linear resonant wave–wave interaction (triad): Case
741 studies based on rocket data and first application to satellite data. *Journal of atmospheric and*
742 *solar-terrestrial physics*, 68(9), 959-976.

743

744 Wüst, S., Offenwanger, T., Schmidt, C., Bittner, M., Jacobi, C., Stober, G., Yee, J.H.,
745 Mlynczak, M. G. & Russell III, J. M. (2018). Derivation of gravity wave intrinsic parameters
746 and vertical wavelength using a single scanning OH (3-1) airglow spectrometer. *Atmospheric*
747 *Measurement Techniques*, 11(5), 2937-2947.

748

749 Smets, P.S.M., Evers, L.G. (2014). The life cycle of a sudden stratospheric warming from
750 infrasonic ambient noise observations, *J. Geophys. Res. Atmos.*, 119, 12,084-12,099

751 Spurr, R., Loyola, D., Heue, K. P., Van Roozendaal, M., & Lerot, C. (2022). S5P/TROPOMI
752 Total Ozone ATBD. Deutsches Zentrum für Luft- und Raumfahrt (German Aerospace
753 Center), Weßling, Germany, Tech. Rep. S5P-L2-DLR-ATBD-400A.

754 Sutherland, L.C., Bass, H.E., (2004). Atmospheric absorption in the atmosphere up to 160
755 km. *J. Acoust. Soc. Am.*, 115, 1012–1032. <https://doi.org/10.1121/1.1631937>

756 Szuberla, C.A.L., Olson, J.V., (2004). Uncertainties associated with parameter estimation in
757 atmospheric infrasound rays. *J. Acoust. Soc. Am.* 115, 253-258. doi: 10.1121/1.1635407

758 Veefkind, J. P., Aben, I., McMullan, K., Förster, H., De Vries, J., Otter, G., ... & Levelt, P. F.
759 (2012). TROPOMI on the ESA Sentinel-5 Precursor: A GMES mission for global
760 observations of the atmospheric composition for climate, air quality and ozone layer
761 applications. *Remote sensing of environment*, 120, 70-83.

762

763